Aliasing artifacts in computerized tomography

C. R. Crawford and A. C. Kak

Streaking artifacts in tomographic images reconstructed by the filtered-backprojection algorithm are caused by aliasing errors in the projection data. To show this a computer simulation study was performed in which the transforms of undersampled projections were subtracted from the corresponding transforms when the projection data were taken with a very large number of rays. This yielded the aliased spectrum for the undersampled case. An image was reconstructed from the difference transforms. Streaks present in this image exactly matched those present in the undersampled reconstruction. (The number of projections used in this study was large enough to preclude any artifacts caused by their insufficient number.) We have derived a theoretical upper bound for the energy contained in these aliasing artifacts. In this paper we have also briefly touched upon the artifacts caused by other algorithmic aspects of a tomographic system.

I. Introduction

The mathematics necessary to obtain tomographic reconstructions from integral projection data using filtered-backprojection techniques has been known for many years.[1] In a computer implementation two unrealistic conditions must be satisfied to obtain exact images. One is that an infinite number of projections is needed, and the second is that the data have to be sampled at infinitely small invervals. An approximate image can be formed if only a finite number of projections, sampled at a finite number of points, are used. It is this deviation from the theory that this paper will address. It should be noted that only algorithm dependent artifacts will be considered. Implementation artifacts, such as beam refraction for the ultrasonic case, and polychromaticity (beam hardening) and photon noise for the x-ray case will not be discussed because, loosely speaking, they are independent of the algorithm artifacts. For a recent discussion of many of the implementation artifacts the reader is referred to Ref. 2.

II. Conventional Approximations

In this section the often used approximations needed to implement the filtered-backprojection algorithm in a discrete environment will be described. Our discussion here will focus on reconstructions from the parallel projection data.

The authors are with Purdue University, School of Electrical Engineering, West Lafayette, Indiana 47907.

Consider a 2-D function $g(x,y)$. A parallel projection at angle θ is given by

$$P(\theta,t) = \int_{-\infty}^{\infty} \int_{-\infty}^{\infty} g(x,y)\delta(x\cos\theta + y\sin\theta - t)dxdy. \quad (1)$$

If the projections are known for all θ between zero and π, the function can be exactly reconstructed by backprojecting filtered versions of the projections. The filtered projections are given by

$$Q(\theta,t) = \int_{-\infty}^{\infty} S(\theta,f)|f| \exp(j2\pi ft)df, \quad (2)$$

where $S(\theta,f)$ is the Fourier transform of $P(\theta,t)$ given by

$$S(\theta,f) = \int_{-\infty}^{\infty} P(\theta,t) \exp(-j2\pi ft)dt. \quad (3)$$

The operation of backprojection for reconstructing $g(x,y)$ is described by

$$g(x,y) = \int_{0}^{\pi} Q(\theta,x\cos\theta + y\sin\theta)d\theta. \quad (4)$$

Equation (4) presupposes that an infinite number of projections from 0 to π are known. Equations (2) and (3) imply that the projections are known at an infinitely small sampling interval. To reduce the amount of information the following assumptions are made.

Instead of trying to obtain the tomogram for the entire plane only a circle of radius T is reconstructed. Distortions occur if the image is not zero outside of this region. Most applications have the object to be scanned immersed in air or water. The projection data are normalized to zero for ray paths that include only the air or water. This simplification will cause no problems unless the projections are not properly normalized.[3]

Since the image is zero outside the circle the projections, $P(\theta,t)$, are also zero for $|t| > T$. To obtain the

exact image an infinite number of samples are needed over the interval $|t| \leq T$. If the projections are approximately bandlimited, $S(\theta,f) \simeq 0$ for $|f| > B$, then if more than $4BT$ samples are used practically all the significant information about the projections can be recovered using the sampling theorem. Let N be the number of samples. The samples, $P_s(\theta,i)$, can be related to the original projection as follows:

$$P_s(\theta,i) = P\left(\theta, -T + \frac{\tau}{2} + i\tau\right); \quad i = 0,1,\ldots,N-1; \quad \tau = \frac{2T}{N} \cdot \quad (5)$$

To obtain the sample locations we first divide the interval $2T$ into N parts each of width τ. The samples are located at the midpoints of these intervals.

If the projections are assumed to be of finite bandwidth B and finite order (which means that the entire bandlimited signal may be represented by a finite number of samples taken at the Nyquist rate), the samples $Q_s(\theta,i)$ of the filtered projections, $Q(\theta,t)$, can be obtained from the sampled projections by replacing the Fourier integrals in Eqs. (2) and (3) by discrete Fourier transforms. This procedure is outlined in Ref. 3, and the result is

$$Q_s(\theta,i) = \frac{1}{N} \sum_{k=-N/2}^{N/2-1} S_s(\theta,k) \left| k \frac{2B}{N} \right| \exp\left(j2\pi \frac{ik}{N}\right), \quad (6)$$

where $S_s(\theta,k)$ is the discrete Fourier transform of $P_s(\theta,i)$:

$$S_s(\theta,k) = \sum_{i=0}^{N-1} P_s(\theta,i) \exp\left(-j\frac{2\pi}{N} ik\right) \cdot \quad (7)$$

Note that Eq. (6) implies a circular convolution between the sampled projection data and the inverse discrete Fourier transform of the sequence $|k[(2B)/N]|$ for $k = -(N/2),\ldots,0,\ldots,(N/2) - 1$ (assuming N is an even number). Equations (6) and (7) can be evaluated using fast Fourier transforms (FFT). Crawford and Kak[4] have shown that because of aliasing of the filter in the space domain, Eqs. (6) and (7) will cause a dc shift and dishing similar to beam hardening in the final reconstruction.

An alternative implementation is obtained by only invoking the assumption of finite bandwidth. Now since the projections are bandlimited, it does not matter what the filter in Eq. (2) is for $|f| > B$. Letting it be zero

$$H(f) = \begin{rcases} = |f|, & |f| \leq B \\ = 0, & \text{elsewhere} \end{rcases} \cdot \quad (8)$$

This corresponds to the following impulse response in the spatial domain:

$$h(t) = \frac{B \sin 2\pi Bt}{\pi t} - \left(\frac{\sin \pi Bt}{\pi t}\right)^2 \cdot \quad (9)$$

If everything is sampled at the Nyquist rate, $\tau = 1/(2B)$, one can show using Eq. (2) that the samples of the filtered projections are given by

$$Q_s(\theta,i) = \tau \sum_{l=-\infty}^{\infty} P_s(\theta,i-l) h_s(l)$$

$$= \tau \sum_{l=-(N-1)}^{N-1} P_s(\theta,i-l) h_s(l) \quad i = 0,1,\ldots,N-1, \quad (10)$$

where the second equality follows from the fact that each sampled projection P_s is zero outside the range $(0, N-1)$ for its index. The sampled function $h_s(l)$ is obtained by substituting $t = l\tau$ in Eq. (9):

$$\begin{rcases} h_s(l) = B^2, & l = 0 \\ = 0, & l \text{ even} \\ = -\frac{4B^2}{l^2\pi^2}, & l \text{ odd} \end{rcases} \cdot \quad (11)$$

Equation (10) implies that in order to know $Q_s(\theta,t)$ exactly at the sampling points the length of the sequence $h_s(l)$ used should be from $l = -(N-1)$ to $l = (N-1)$. It is important to realize that the results obtained by using Eq. (10) are not identical to those obtained by using Eq. (7). This is because the discrete Fourier transform of the sequence $h_s(l)$ with l taking values in a finite range [such as when l ranges from $-(N-1)$ to $(N-1)$] is not the sequence $|k[(2B)/N]|$. While the latter sequence is zero at $k = 0$, the DFT of $h_s(l)$ with l ranging from $-(N-1)$ to $(N-1)$ is nonzero at this point.

The discrete convolution in Eq. (10) may be implemented directly on a general purpose computer. However, it is much faster to implement it in the frequency domain using FFT algorithms. [By using specially designed hardware, direct implementation of Eq. (10) can be made as fast or faster than the frequency domain implementation.] For the frequency domain implementation one has to keep in mind the fact that one can now only perform periodic (or circular) convolutions. The convolution required in Eq. (10) is aperiodic. To eliminate the interperiod interference artifacts inherent to periodic convolution we pad the projection data with a sufficient number of zeros. It can easily be shown[5] that if we pad $P_s(i)$ with zeroes so that it is $(2N-1)$ elements long, we avoid interperiod interference over the N samples of Q_s. Of course, if one wants to use the base 2 FFT algorithm, which is most often the case, the sequences P_s and h_s have to be zero-padded so that each is $(2N-1)_2$ elements long, where $(2N-1)_2$ is the smallest integer that is a power of 2 and that is greater than $2N-1$. Therefore, the frequency domain implementation may be expressed as

$$Q_\theta(n\tau) = \tau \times \text{IFFT}\{\text{FFT}\{P_\theta(n\tau) \text{ with } ZP\}$$
$$\times \{\text{FFT}h(n\tau) \text{ with } ZP\}\}, \quad (12)$$

where FFT and IFFT denote, respectively, fast Fourier transform and inverse fast Fourier transform; ZP stands for zero padding. One usually obtains superior reconstructions when some smoothing is also incorporated in Eqs. (10) or (12). For example, in Eq. (12) smoothing may be implemented by multiplying the product of the two FFTs by a Hamming window.

The unsampled filtered projection, $Q(\theta,t)$, can be recovered exactly by low-pass filtering. In practice this is too computationally expensive, and linear interpolation is used. The relation is
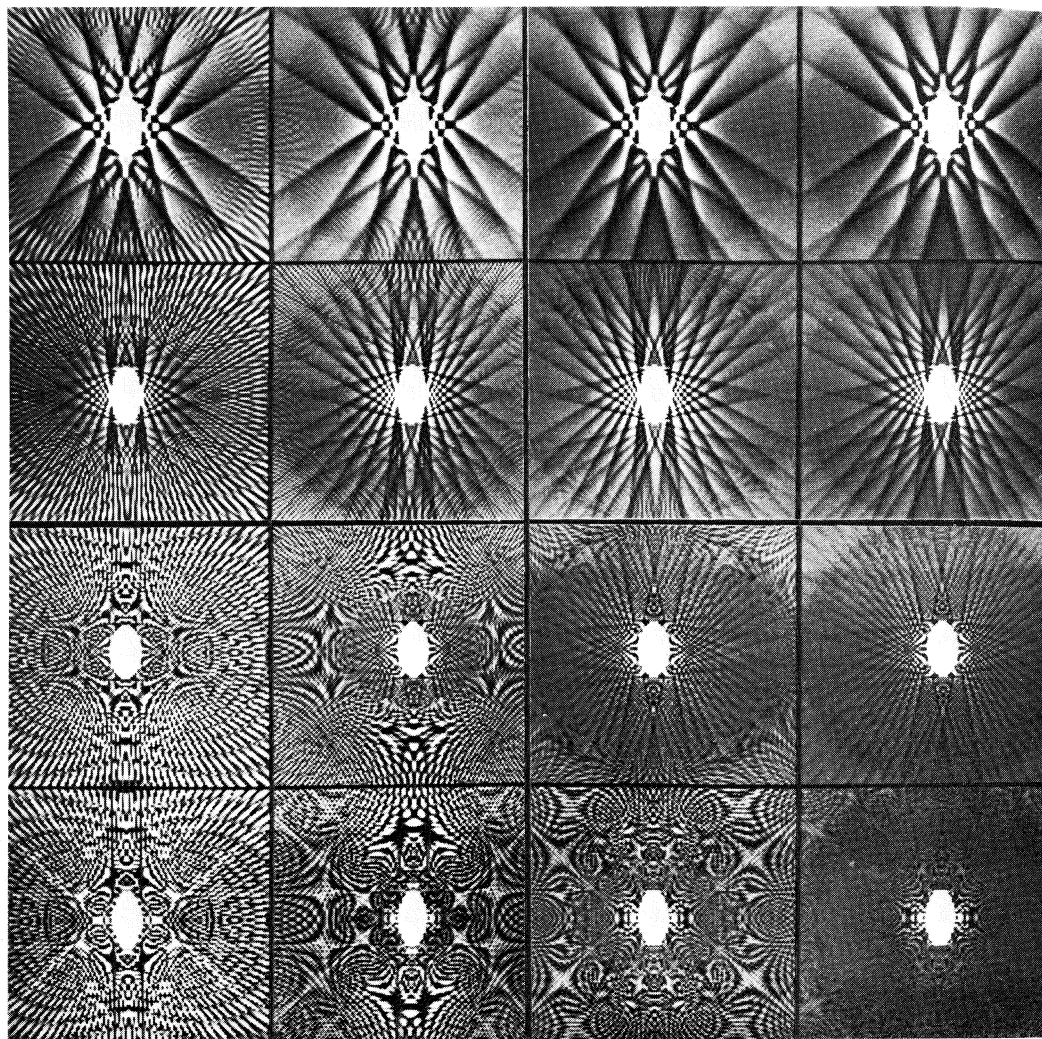
Fig. 1.   Sixteen reconstructions of an ellipse for various values of K and N.   The reconstructions were windowed for the purpose of display to bring out the aliasing streaks and moiré artifacts.

$$Q'(\theta,t) = (\alpha - [\alpha])Q_s(\theta,[\alpha]) + (1 - \alpha + [\alpha])Q_s(\theta,[\alpha] + 1)$$
$$\alpha = \frac{t + T - (\tau/2)}{\tau} \Bigg\} , \quad (13)$$

where Q' is a linearly interpolated approximation to Q, and $[\alpha]$ is the greatest integer less than or equal to α.

The next simplification is the replacement of the integral in Eq. (4) with a summation. This is needed because in any real system there can only be a finite number of projections. If there are K equally spaced

projections, using Eqs. (4) and (13) we get for the reconstructed image $g'(x,y)$

$$g'(x,y) = \frac{\pi}{K} \sum_{i=0}^{K-1} Q'(\theta_i, x\cos\theta_i + y\sin\theta_i)$$
$$\theta_i = i\frac{\pi}{K} \Bigg\} , \quad (14)$$

This approximation works well when the number of projections is large, which is usually the case in most tomographic imaging systems.   If one has only a limited

number of projections there may be better approximations.[6]

Equation (14) is valid for any point (x,y), but only a finite number of picture points can be reconstructed in a computer implementation. Since the picture is zero outside of a circle of radius T only a square of dimensions $2T$ by $2T$ will be considered. This will be sampled at M^2 points. The discrete reconstructed image, denoted by g_s, is then related to $g'(x,y)$ as follows:

$$g_s(m,n) = g'\left(-T + \frac{\delta}{2} + m\delta, \ -T + \frac{\delta}{2} + n\delta\right), \qquad (15)$$
$$m,n = 0,1,\ldots,M-1$$

where $\delta = (2T)/M$.

In summary, these approximations have been made: the projections are spatially limited and bandlimited; the filtered projections can be recovered using linear interpolation; a finite number of projections can be used to make an accurate reconstruction; and the final image can be represented by a finite number of points.

III. Effects of the Approximations

Figure 1 shows sixteen windowed reconstructions of an ellipse with various values of K (number of projections) and N (number of samples per projection). Figure 2 is a graphical depiction of the numerical values on the middle horizontal lines through two of the reconstructions. The following degradations are evident: Gibbs phenomenon, streaks, and moiré patterns. These effects will now be related to the approximations made in the previous section.

A fundamental problem with these images and in general any tomographic pictures is that usually the objects are not bandlimited. When a nonbandlimited

function is sampled or when a bandlimited function is sampled below its Nyquist rate, the portion of the spectrum above the Nyquist frequency is folded back into the lower frequencies. This causes the function to be bandlimited and also have aliasing errors in it.

Backprojection is a linear process so the final image can be thought to be made up of two functions. One is the image made from the bandlimited projections degraded by linear interpolation and the finite number of projections. The second is the image made from the aliased portion of the spectrum in each projection.

The aliased portion of the reconstruction can be seen by itself by subtracting the transforms of the sampled projections from the corresponding theoretical transforms of the original projections. Then if this result is filtered as before the final reconstructed image will be that of the folded over spectrum. We performed a computer simulation study along these lines for an elliptical object. In order to present the result of this study we first show in Fig. 3(a) the reconstruction of an ellipse for $N = 64$. (The number of projections was 512 and will remain the same for the discussion here.) We subtracted the transform of each projection for the $N = 64$ case from the corresponding transform for $N = 1024$ case. The latter was assumed to be the true transform because the projections are oversampled (at least in comparison with the $N = 64$ case). The reconstruction obtained from the difference data is shown in Fig. 3(b). Figure 3(c) is the bandlimited image obtained by subtracting the aliased spectrum image of Fig. 3(b) from the complete image shown in Fig. 3(a). Figure 3(c) is the reconstruction that would be obtained provided the projection data for the $N = 64$ case were truly band-limited (i.e., did not suffer from aliasing errors after sampling). The aliased-spectrum recon-
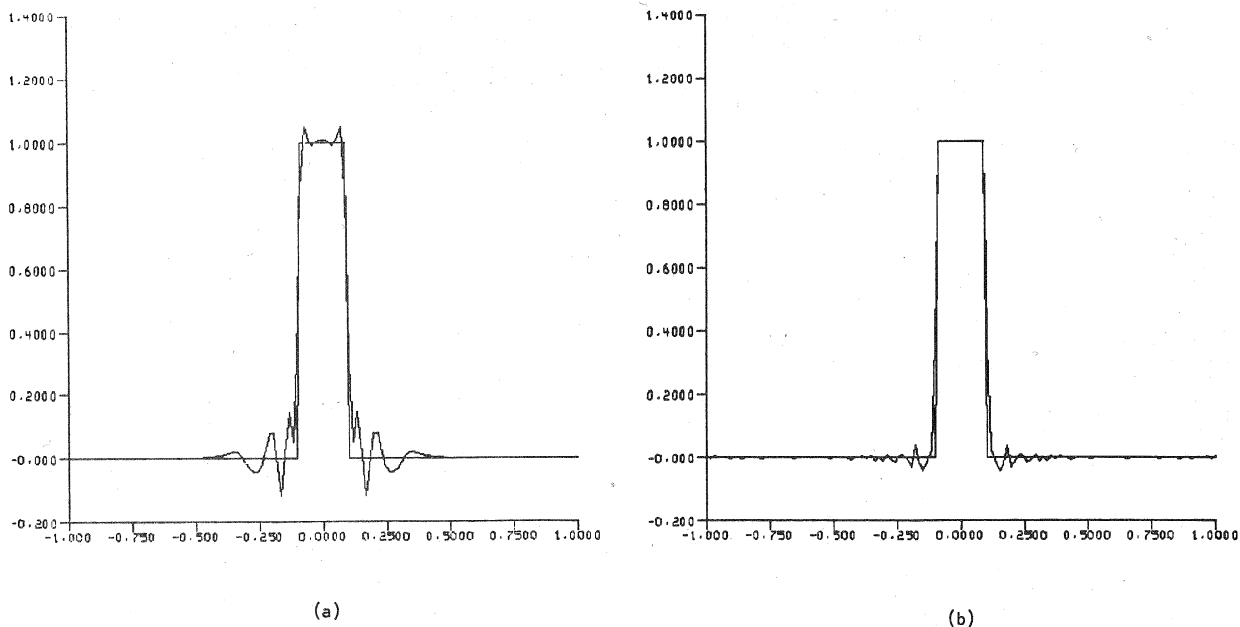

(a)

(b)

Fig. 2.   This figure is a graphical depiction of the numerical values on the middle horizontal lines in two of the reconstructions in Fig. 1. The jagged lines are the reconstructed values while the straight lines are the true values: (a) $N = 64$, $K = 512$; (b) $N = 512$, $K = 512$.
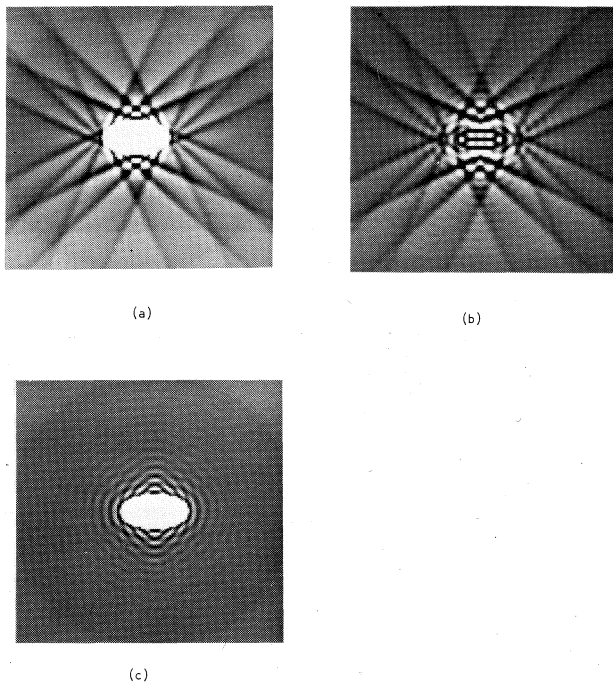
Fig. 3.   (a) Reconstruction of an ellipse with $N = 64$ and $K = 512$.   (b) Reconstruction from only the aliased frequencies in each projection. Note that the streaks exactly match those in (a).   (c) Image obtained by subtracting (b) from (a). This is the reconstruction that would be obtained provided the data for the $N = 64$ case were truly bandlimited.

struction in Fig. 3(b) and the absence of streaks in Fig. 3(c) prove our point that when the number of projections is large, the streaking artifacts are caused by aliasing errors in the projection data.

Imaging systems are often characterized by their point spread functions (PSF). For linear position-invariant systems such a characterization is generally considered to be complete. However, for sampled systems this is not always true. Often the PSF will give no indication of object-spectra dependent artifacts such as the aliasing streaks discussed above. For example, for the $K = 512$, $N = 64$ case, the PSF is shown in Fig. 4(b), while the reconstruction of the ellipse for the same K and N is shown in the upper right-hand corner of Fig. 1. While the PSF looks nice and smooth, the aliasing streaks are quite evident in the ellipse reconstruction. [The PSFs in Fig. 4 were generated for a point source located at the origin. Also, for each projection the $(N/2)$th ray passed through the origin.]

The distortions that one can see in the PSF are those that are totally intrinsic to the algorithm such as would be caused by an inadequate number of projections, the effect of interpolation (which like aliasing depends upon N), and the display grid not being fine enough.

The system will yield perfect images (in the absence of aliasing) if the PSF has a single value at the origin and zero everywhere else. Because of the finite bandwidth, if K is infinite, the PSF will be the inverse Hankel transform of a disk of radius B. That is, the PSF, denoted by $h(x,y)$, will now be given by the function

$$h(x,y) = [BJ_1(2\pi Br)]/r, \qquad (16)$$

where $r = (x^2 + y^2)^{1/2}$. Clearly, the width of the main lobe is inversely related to the projection bandwidth B. This is also illustrated in Fig. 4 where the PSF for the $N = 64$ case has a wider main lobe than that for the $N = 512$.

Along with the main lobes, other structured noise can also be seen in some of the PSFs in Fig. 4. Brooks[6] has shown that this noise is caused by a finite K. He also showed that if K is larger than $[(1.1\pi)/4] N$, the PSF is essentially noise free. This is confirmed in Fig. 4. It was shown by Shepp and Logan[7] that for a finite K and infinite N the noise caused by the finite number of projections will go to infinity.

The effects of interpolation can be combined into the PSF. Oppenheim[8] has shown that interpolation can be seen as convolving the unsampled projection with a window. Thus by the Fourier slice theorem, the Fourier transform of the PSF without interpolation is multiplied by the Fourier transform of the window rotated about the origin. The PSFs presented in Fig. 4 already include the effects of interpolation. Because different interpolation windows effect the spectrum differently, they could enhance or suppress the aliasing errors. This has led some authors[9] to attribute aliasing streaks to interpolation errors.

The last degradation in the images is moiré patterns.[10]   These can be seen in Fig. 1 where $N = 512$ and $K = 64$. The projection data now have a large bandwidth. However, the display grid is not fine enough to represent these high frequencies and 2-D aliasing takes place. It is interesting to note that two different types of aliasing artifacts may occur in computerized tomog-
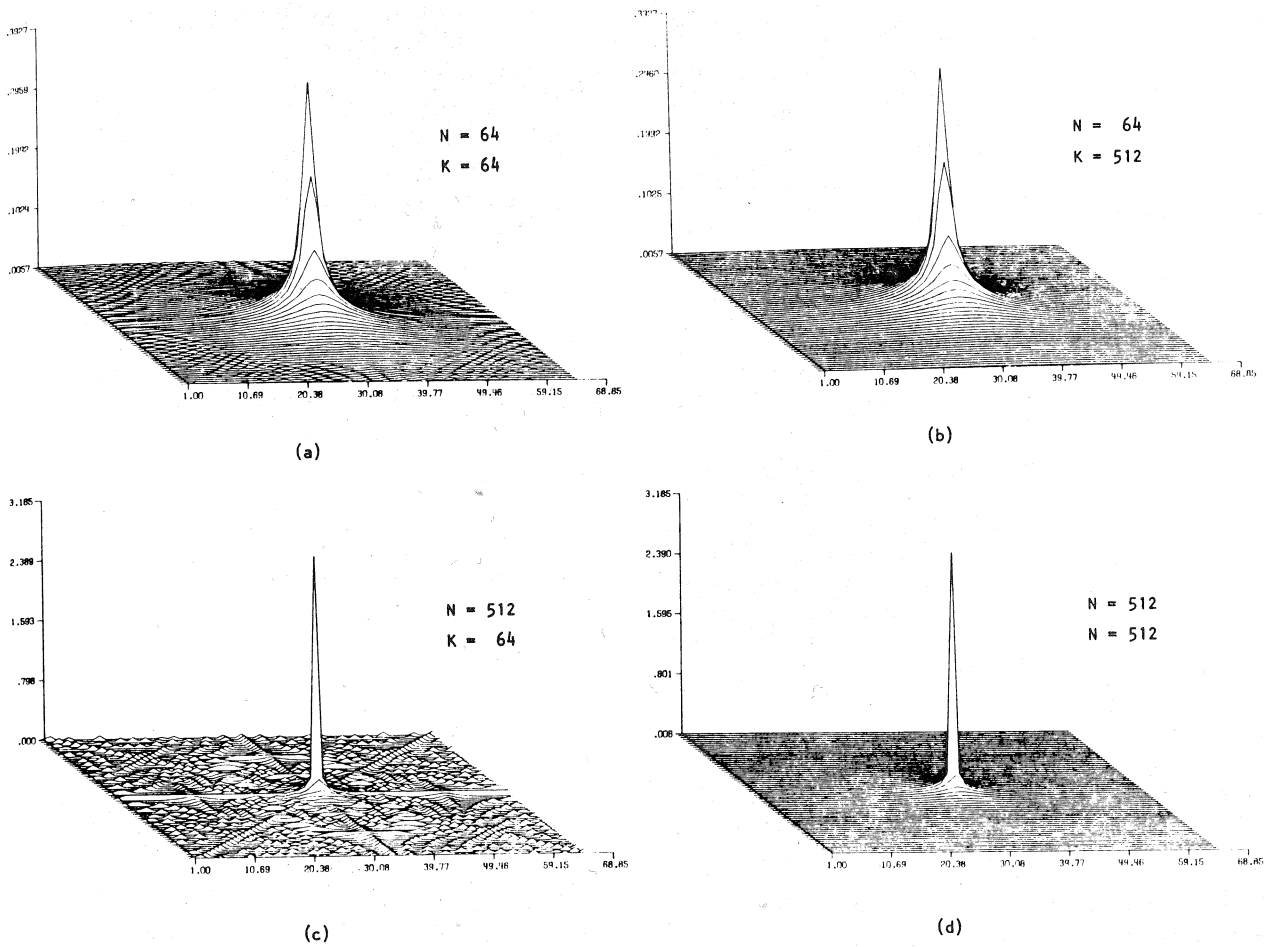
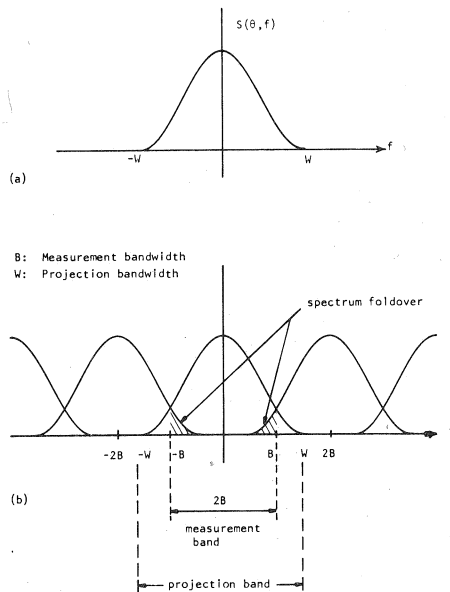**Fig. 4.** Point spread functions for some of the reconstructions in Fig. 1.

Fig. 5. (a) A symbolic depiction of the aliasing distortion. $S(\theta,f)$ is the transform of the true projection at angle θ. (b) Some of the replication of $S(\theta,f)$ are shown here. The sum of these replications is $\bar{S}(\theta,f)$.

raphy: those caused by undersampling of the projection data and those caused by the display grid not being fine enough.

IV. Upper Bound for Energy in Aliasing Streaks

In this section an upper bound for the energy in the streaks for an elliptical object will be found assuming an infinite number of projections. Our interest in elliptical objects stems from the mathematical tractability of this case and, also, because of their frequent use in computer simulation work in tomography.

Let $\widehat{S}(\theta,f)$ be the Fourier transform of the samples of the projection at angle θ. It is related to the true transform by

$$\widehat{S}(\theta,f) = \sum_{i=-\infty}^{\infty} S(\theta,f-2iB), \qquad (17)$$

where $B = \frac{1}{2}\tau$, τ being the sampling interval. Note that with the sampling interval τ, B is the measurement bandwidth of the system. Both $\widehat{S}(\theta,f)$ and $S(\theta,f)$ are illustrated in Fig. 5. For most cases of aliasing distortion the measurement bandwidth B is only slightly less than the projection bandwidth W, which is the case depicted in the figure. Now let $S^A(\theta,f)$ denote the aliased frequency components within the measurement bandwidth. It is clear from Fig. 5 that $S^A(\theta,f)$ consists essentially of contributions made by the two, the first left and the first right, replications of the baseband spectrum. Thus we may write

$$S^A(\theta,f) = S(\theta,f-2B) + S(\theta,f+2B), \qquad |f| < B. \qquad (18)$$

Let $g^A(x,y)$ denote the reconstruction from only the aliased frequencies. The total energy in this reconstruction will be denoted by E^A and may be defined as

$$E^A = \int_{-\infty}^{\infty} \int_{-\infty}^{\infty} |g^A(x,y)|^2 dxdy. \qquad (19)$$

Using the Fourier slice theorem and Parseval's theorem, Eq. (19) becomes

$$E^A = \int_0^{\pi} \int_{-\infty}^{\infty} |S^A(\theta,f)|^2 |f| dfd\theta. \qquad (20)$$

Since we are interested in aliased frequencies within the measurement band only we may write

$$E^A = \int_0^{\pi} \int_{-B}^{B} |S^A(\theta,f)|^2 |f| dfd\theta. \qquad (21)$$

Now an object consisting of a single ellipse at the origin of major and minor axes given by $2R$ and $2S$, respectively, is mathematically described by

$$\left. \begin{array}{l} g(x,y) = 1, \quad \dfrac{x^2}{R^2} + \dfrac{y^2}{S^2} \leq 1 \\[2mm] \qquad = 0, \quad \text{elsewhere} \end{array} \right\}. \qquad (22)$$

The projections, $P(\theta,t)$, of this object are given by

$$\left. \begin{array}{l} P(\theta,t) = \dfrac{2RS}{a^2}(a^2-t^2)^{1/2}, \quad |t| \leq a \\[2mm] \qquad = 0, \qquad\qquad\qquad \text{elsewhere} \end{array} \right\}, \qquad (23)$$

where $a^2 = R^2 \cos^2\theta + S^2 \sin^2\theta$. The Fourier transform of $P(\theta,t)$ is given by

$$S(\theta,f) = \frac{RS}{a} \frac{J_1(2\pi af)}{f}, \qquad (24)$$

where $J_1(\cdot)$ is the Bessel function of order one.

Near $f = B$ and $f = -B$ the function $[J_1(x)]/x$ can be well approximated by its asymptotic form:

$$\frac{J_1(x)}{x} \simeq \left(\frac{2}{\pi |x|^3}\right)^{1/2} \cos\left(|x| - \frac{3\pi}{4}\right) \qquad x \to \infty \quad \text{or} \quad x \to -\infty. \qquad (25)$$
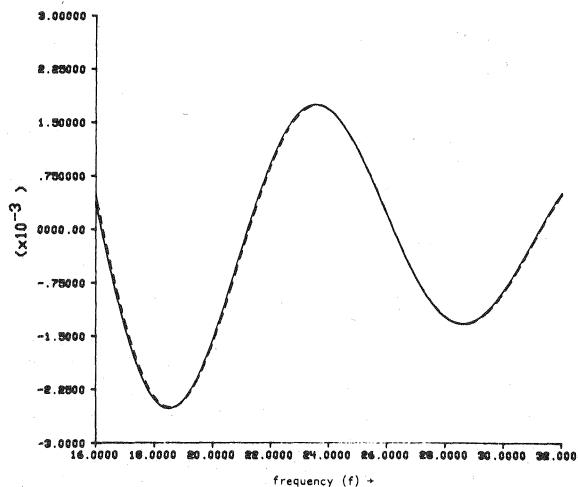
Fig. 6.   This figure illustrates the fact that beyond the limits of the measurement bandwidth in the frequency domain, the Bessel function can be well approximated by its asymptotic form. (In this case the measurement band is from $f = -16$ to $f = 16$.) The solid curve corresponds to the exact result obtained by using Eq. (24); and the dashed curve is based on the approximation in Eq. (25).

To illustrate the reasonableness of this approximation consider the case of the ellipse in Fig. 3 whose dimensions are given by $R = 0.2$ and $S = 0.1$. Now let us select $a = 0.1$ since this corresponds to the projection with the maximum bandwidth. Let us say we have 64 samples per projection and let the value of T be 1. Therefore, $\tau = 2/64$ and $B = \frac{1}{2}\tau = 16$. Hence the measurement band is given by $-16 < f < 16$. The solid curve in Fig. 6 is a plot of $S(\theta,f)$ as given by Eq. (24) for $16 < f < 32$; and the dashed curve is obtained by using the approximation in (25). Since in our experiments the 64 samples represent a highly undersampled case, and since the asymptotic approximation gets better as N is increased, using (25) is a good approximation for discussing aliasing. Using (24) and (25) we write for $s(f - 2B)$ at frequencies $f < B$:

$$S(\theta, f - 2B) \simeq \frac{RS}{\pi[a(2B - f)]^{3/2}} \cos\left[2\pi a(2B - f) - \frac{3\pi}{4}\right]$$
$$\text{for} \quad f < B. \quad (26)$$

A similar asymptotic expression can be written for $S(f + 2B)$ at frequencies $f > -B$:

$$S(\theta, f + 2B) \simeq \frac{RS}{\pi[a(2B + f)]^{3/2}} \cos\left[2\pi a(2B + f) - \frac{3\pi}{4}\right]$$
$$\text{for} \quad f > -B. \quad (27)$$

We will now assume that the measurement bandwidth is large enough so that in the baseband spectrum frequencies above $2B$ do not contribute to aliasing. That is, for practical purposes we may write $B < W < 2B$. [Note that this assumption is consistent with ours including only two replications in Eq. (18).] Therefore, we can ignore the energy in $S(\theta, f - 2B)$ and $S(\theta, f + 2B)$ at frequencies $f < 0$ and $f > 0$, respectively. With this assumption substitution of (26) and (27) in (18) leads to

$$S^A(\theta, f) = \frac{RS}{\pi[a(2B - |f|)]^{3/2}} \cos\left[2\pi a(2B - |f|) - \frac{3\pi}{4}\right]. \quad (28)$$

Substituting Eq. (28) into Eq. (21)

$$E^A \simeq \frac{4(RS)^2}{\pi^2} \int_0^{\pi/2} \frac{1}{a^3} d\theta \int_0^B \frac{f\cos^2\left[2\pi a(2B - f) - \frac{3\pi}{4}\right]}{(2B - f)^3} df. \quad (29)$$

The inner integral can be reduced to

$$\frac{1}{8B} - \frac{1}{2}\int_B^{2B} (2Bz^{-3} - z^{-2})\sin(4\pi az)dz. \quad (30)$$

The integral in (30) can be bounded in absolute value by $1/(4B)$ so the integral in (29) reduces to

$$E^A \leq \frac{(RS)^2}{\pi^2 B} \int_0^{\pi/2} a^{-3}(\theta)d\theta. \quad (31)$$

The integral in (31) can be evaluated using identities found in Ref. 11.

$$E^A \leq \frac{R}{\pi^2 B} E[\beta], \quad (32)$$

where $\beta = (1 - (S/R)^2)^{1/2}$ and where $E[x]$ is an elliptic integral defined as

$$E[x] = \int_0^\pi (1 - x^2\sin^2\alpha)^{1/2}d\alpha. \quad (33)$$

The value of the upper bound in (31) [or (32)] lies in its functional dependence on the parameters of the size of the ellipse. This upper bound led us to an interesting conclusion (verified eventually by computer simulation) that although a larger ellipse is more low-frequency in character, the energy in its aliasing streaks should be greater. The intuitive justification for this is the fact that as an ellipse gets larger, in its frequency domain representation its energy increases at all frequencies including those that contribute to aliasing. The reader may note that for any give S/R as an ellipse is made larger, although E^A increases, the normalized streak energy given by $E^A/\pi RS$ will decrease. The factor πRS is the energy in the ellipse itself. Also (31) [or (32)] lead to the expected conclusion that the energy in the streaks is bounded from above by a function that is inversely related to the bandwidth, which implies that it is inversely related to the number of sample points. This is seen in Fig. 1 in the last column where the streaks die out as N increases.

V. Conclusions

In computerized tomography based on filtered-backprojection algorithms, streaks are caused by aliasing errors introduced when the projection data are undersampled. These aliasing streaks are different from (and, in addition to) the streaks caused by an insufficient number of projections.

References

1. R. N. Bracewell and A. C. Riddle, Astrophys. J. **150**, (1967).
2. A. C. Kak, "Computerized Tomography with X-ray, Emission and Ultrasound Sources," to appear in Proc. IEEE **67**, (Sept. 1979).
3. A. C. Kak, C. V. Jakowatz, N. Baily, and R. Keller, IEEE Trans. Biomed. Eng. **BME-24**, 157 (1977).
4. C. R. Crawford and A. C. Kak, "Aliasing Artifacts in CT Images," School of Electrical Engineering, Purdue University, Research Report TR-EE 79-25 (December 1978).
5. C. V. Jakowatz and A. C. Kak, "Computerized Tomography Using X-rays and Ultrasound," School of Electrical Engineering, Purdue University, Research Report TR-EE 76-26, July 1976.
6. R. A. Brooks, G. H. Weiss, and A. J. Talbert, J. Comput. Assisted Tomog. **12**, 577 (Nov. 1978).
7. L. A. Shepp and B. F. Logan, IEEE Trans. Nucl. Sci. **NS-21**, 21 (June 1974).
8. B. E. Oppenheim, "Reconstruction Tomography from Incomplete Projections," in *Reconstruction Tomography in Diagnostic Radiology and Nuclear Medicine*, M. M. Ter-Pogossian, Ed. (University Park Press, University Park, Pa. 1977), pp. 155–183.
9. H. P. Weiss and J. A. Stein, "The Effect of Interpolation in CT Image Reconstruction," in *Proceedings IEEE Conference on Pattern Recognition and Image Processing, Chicago*, May 1978, p. 193.
10. A. Rosenfeld and A. C. Kak, *Digital Picture Processing* (Academic, New York, 1976).
11. I. S. Gradshteyn and I. M. Ryzhik, *Table of Integrals, Series, and Products* (Academic, New York, 1965), p. 156.